Uncertainty-Guided Conservative Propagation for Coronary Artery Segmentation

Huan Huang[1[0009−0004−3988−762X]], Zhihui Xu[2], Michele Esposito[3], and Chen Zhao[1[0000−0002−5782−3329]⋆]

[1] Department of Computer Science, Kennesaw State University, Marietta, GA 30060, USA
[2] The First Affiliated Hospital of Nanjing Medical University, Nanjing 211166, China
[3] Department of Cardiology, Medical University of South Carolina, Charleston, SC 29425, USA

Abstract. Accurate coronary artery segmentation plays a critical role in coronary artery disease diagnosis and treatment planning. However, existing deep learning approaches are predominantly formulated as point-wise classification paradigms, where predictions are produced in a single forward pass without an explicit inference-stage structured update mechanism. This limitation becomes particularly evident in regions with ambiguous image evidence or weak structural support. We propose an Uncertainty-Guided Conservative Propagation (UGCP) framework that reformulates segmentation inference as a finite-step, structure-aware state evolution process in logit space via constrained neighborhood updates guided by conservative-inspired local interaction. The update is driven by local prediction discrepancies and modulated by voxel-wise uncertainty, allowing high-confidence regions to guide structurally unstable areas in a controlled manner. A source term anchors the update to the initial logits, preventing excessive drift during structural correction. We evaluate the proposed framework on convolutional and Transformer-based segmentation backbones using public 2D invasive coronary angiography (ICA) and 3D coronary CT angiography (CCTA) datasets (616 ICA images and 1,000 CCTA volumes). Experimental results demonstrate consistent improvements in the Dice similarity coefficient (DSC), clDice, and boundary metrics across architectures. The proposed framework enhances inference-stage structural consistency and shows potential for improving the robustness of coronary artery analysis. Our code is available at: `https://github.com/chenzhao2023/UGCP`.

Keywords: Coronary Artery Segmentation · Uncertainty Quantification · Conservative Propagation

1 Introduction

Coronary artery segmentation plays a fundamental role in cardiovascular disease assessment, as it enables precise delineation of arterial structure and plaque-

⋆ Corresponding author: `czhao4@kennesaw.edu`.

related narrowing, supporting accurate assessment of disease severity and informed clinical decision making [7,23]. Unlike conventional organ segmentation, cardiovascular structures exhibit elongated tubular morphology and strong structural dependency, making predictions highly sensitive to connectivity and branch integrity [11,21]. Even when global overlap metrics are high, local branch discontinuities or spurious connections can significantly affect downstream functional analysis and quantitative evaluation [28,27]. Therefore, coronary artery segmentation concerns not only regional accuracy, but also structural coherence and predictive stability, which continue to pose significant challenges.

Despite significant advances achieved by deep learning approaches in cardiovascular segmentation [13,1,10], mainstream segmentation methods are predominantly formulated as point-wise classification models, where predictions are produced in a single forward pass without an explicit inference-stage structured update mechanism [3,4,24,9]. In regions with ambiguous boundaries or insufficient image evidence, models typically produce deterministic class decisions without explicitly modeling predictive uncertainty, which can lead to over-confident predictions in structurally unstable areas [17]. To mitigate structural inconsistency, prior studies have introduced post-processing strategies or topology-aware losses [16,2,18,25]. However, post-processing methods operate as independent steps detached from the model's prediction mechanism, whereas topology-aware losses primarily influence parameter optimization during training, without modifying the inference-stage decision rule. Meanwhile, uncertainty quantification (UQ) methods can characterize predictive confidence and affect training through loss reweighting or reliability estimation [22,12,6]. Nevertheless, in most implementations, uncertainty information is not integrated into the prediction update mechanism at the inference stage [5,14]. Consequently, existing approaches lack an explicit inference-stage update framework that jointly integrates neighborhood structural interaction and uncertainty-driven regulation.

To address these limitations, we propose an Uncertainty-Guided Conservative Propagation (UGCP) framework that reformulates segmentation inference as a finite-step state evolution process through uncertainty-aware neighborhood interaction. In classical interaction systems, quantities evolve through local exchanges between neighboring states following structured update patterns. Inspired by such conservative interaction principles [15], UGCP models prediction generation as a finite-step discrete update system in logit space. The contributions of this work are threefold: (1) we formulate inference as a conservation-inspired local propagation process with an explicit source term, enabling neighborhood-coupled structural interaction; (2) we introduce uncertainty-modulated propagation to adaptively correct structurally unstable regions; (3) we propose a dimension-agnostic, backbone-independent framework validated on both 2D Invasive Coronary Angiography (ICA) and 3D Coronary CT Angiography (CCTA) datasets using representative convolutional and Transformer-based backbones.

2 Method

2.1 State Update Formulation

Conventional segmentation models produce predictions via point/voxel-wise classification. Given an input image x on a discrete spatial domain $\Omega \subset \mathbb{Z}^d$ with spatial dimension d, a segmentation backbone $\mathcal{B}$ extracts features $h = \mathcal{B}(x)$. A point-wise linear projection $W_s(\cdot)$ is then applied to the initial logits at each spatial location, yielding $s_p^{(0)} = W_s(h_p)$ for every $p \in \Omega$. Under this paradigm, class probabilities are obtained from logits through a standard normalization operation, and prediction is produced in a single forward pass without explicit structural interaction among spatial locations.

As illustrated in Fig. 1, UGCP instead models inference as a finite-step discrete evolution in logit state space. According to the initial logit field $s^{(0)} = \{s_p^{(0)} \mid p \in \Omega\}$ obtained via the projection $s^{(0)} = W_s(h)$, the state evolves through iterative structured updates, as denoted in Eq. (1).

$$s^{(t+1)} = s^{(t)} + \theta\,\mathcal{U}\Big(s^{(t)}\Big), \quad \text{s.t.} \quad t \in \{0, 1, \ldots, T-1\}. \tag{1}$$

where T is the number of update steps, θ is a hyperparameter controlling the step size, and $\mathcal{U}(\cdot)$ is a local spatial operator that aggregates neighborhood interactions in logit space. Thus, the prediction is obtained through the iterative state evolution rather than a single-shot local decision. The terminal state $s^{(T)}$ is subsequently transformed into class probabilities through the Dirichlet expectation to produce the final prediction.

2.2 Evidential Representation and Uncertainty Modeling

To quantify predictive uncertainty during state evolution, we adopt evidential learning [20] and parameterize a Dirichlet distribution whose concentration parameters are derived from the logit state at each iteration. For spatial location $p \in \Omega$ and class index $k \in \{1, \ldots, K\}$, the Dirichlet concentration parameter and its corresponding expected class probability are denoted by $\alpha_{p,k}^{(t)}$ and $\pi_{p,k}^{(t)}$, respectively, as shown in Eq. (2).

$$\alpha_{p,k}^{(t)} = \mathrm{softplus}\Big(s_{p,k}^{(t)}\Big) + 1, \pi_{p,k}^{(t)} = \frac{\alpha_{p,k}^{(t)}}{\sum_{j=1}^{K} \alpha_{p,j}^{(t)} + \varepsilon} \tag{2}$$

where $\varepsilon > 0$ ensures numerical stability. The total concentration reflects the aggregated class evidence, and its inverse naturally defines a continuous uncertainty scalar field, as shown in Eq. (3).

$$u_p^{(t)} = \frac{K}{\sum_{j=1}^{K} \alpha_{p,j}^{(t)} + \varepsilon}. \tag{3}$$

In UGCP, the uncertainty field directly modulates directional gating and source stabilization during iterative updates. The Dirichlet expectation at $t = T$

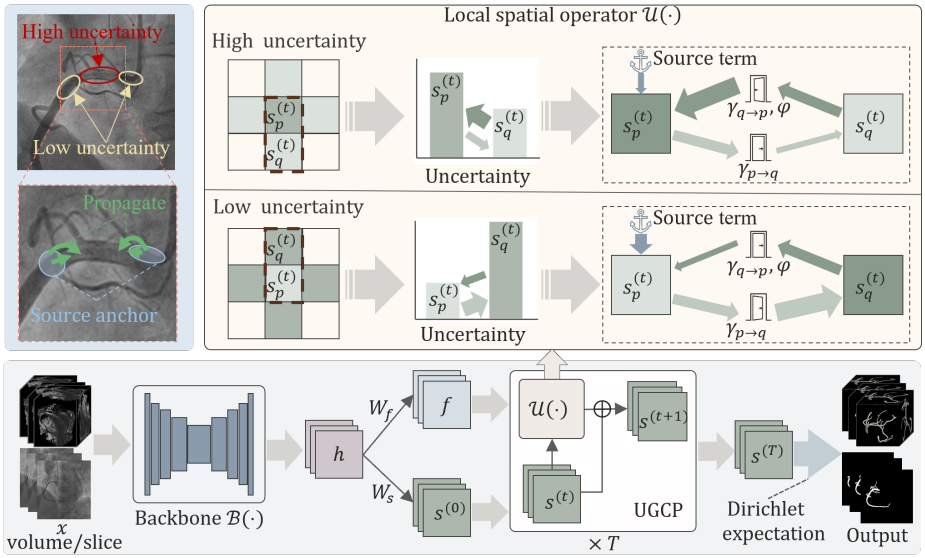

Fig. 1. Overview of UGCP. A 4-neighborhood is used in 2D and extended to a 6-neighborhood in 3D. The arrows illustrate local directional information flow between adjacent spatial locations.

yields the final class probability vector used for segmentation. Unlike entropy computed from normalized probabilities, the Dirichlet concentration is directly derived from logits and jointly encodes evidence magnitude and class proportion, yielding a more stable and propagation-consistent uncertainty measure.

2.3 Uncertainty-Guided Logit Update Operator

We instantiate the local operator $\mathcal{U}(\cdot)$ in Eq. (1) through uncertainty-guided neighborhood interaction with source stabilization.

On the discrete domain Ω, we define the axis-aligned neighborhood $\mathcal{N}(p) = \{\, q \in \Omega \mid \|q - p\|_1 = 1 \,\}$, corresponding to the 4-neighborhood in 2D and the 6-neighborhood in 3D. For adjacent locations p and $q \in \mathcal{N}(p)$, we introduce directional UQ gates as shown in Eq. (4).

$$\gamma_{q\to p}^{(t)} = \sigma\left(\frac{u_p^{(t)} - u_q^{(t)}}{\tau + \varepsilon}\right), \quad \gamma_{p\to q}^{(t)} = \sigma\left(\frac{u_q^{(t)} - u_p^{(t)}}{\tau + \varepsilon}\right) \tag{4}$$

where $\sigma(\cdot)$ denotes the sigmoid function and $\tau > 0$ is a temperature parameter.

This asymmetric gating increases the incoming weight $\gamma_{q\to p}^{(t)}$ when $u_p^{(t)} > u_q^{(t)}$, promoting information flow from more confident to more uncertain locations.

To suppress unreliable cross-boundary propagation, we introduce an edge factor based on an additional feature projection $f = W_f(h)$ that captures local

structural discrepancies beyond logit confidence.

$$\varphi_{p,q} = \tanh\big(w^\top (f_p - f_q)\big)\,, \tag{5}$$

where w is a learnable vector with the same feature dimension as f_p, and f_p, f_q denote decision-aligned features at locations p and q. The edge factor is applied to the incoming component to attenuate unreliable cross-boundary propagation.

We further introduce a source gate to control the activation of the source term, as shown in Eq. (6).

$$r_p^{(t)} = \sigma\left(\frac{u_0 - u_p^{(t)}}{\tau + \varepsilon}\right), \tag{6}$$

where u_0 is a predefined uncertainty threshold. The corresponding source term $r_p^{(t)}\big(s_p^{(0)} - s_p^{(t)}\big)$ anchors the evolving state to the initial logits and prevents excessive deviation during propagation.

Combining the UQ gates, edge factor, and source term, the local operator in Eq. (1) is defined as

$$\mathcal{U}(s_p^{(t)}) = \sum_{q \in \mathcal{N}(p)} \Big(\gamma_{q\to p}^{(t)}\, \varphi_{p,q}\, s_q^{(t)} - \gamma_{p\to q}^{(t)}\, s_p^{(t)}\Big) + r_p^{(t)}\big(s_p^{(0)} - s_p^{(t)}\big). \tag{7}$$

This interaction follows an in–out exchange structure, where the incoming contribution at one location corresponds to an outgoing component at its neighbors, yielding a conservation-inspired local exchange update in the absence of the source term. The source term introduces a controlled non-conservative component that anchors the evolution to the initial logits.

For binary coronary artery segmentation, the update is restricted to the foreground channel, whereas the decision boundary is determined by the foreground–background logit contrast. The resulting operator remains fully differentiable and locally defined, allowing the entire propagation process to be integrated into the segmentation network and optimized in an end-to-end manner.

3 Experiments and Results

3.1 Experimental Setup

We conduct experiments on two public coronary artery segmentation datasets, including the 2D ICA dataset (616 images) [29] and the 3D CCTA dataset (1,000 cases) [26]. ICA images have resolution 512×512 and CCTA volumes have in-plane resolution 512×512 with slice numbers ranging from 206 to 275. All CCTA volumes are resampled to 0.5 mm isotropic spacing. Intensity values are windowed using window level 300 and window width 800 followed by normalization to $[0, 1]$. For ICA, standard data augmentation including random flipping, contrast, and brightness adjustment is used. For CCTA, online random patch sampling with patch size $128 \times 128 \times 128$ is applied, sampling 16 patches per

Table 1. Quantitative comparison on 2D ICA and 3D CCTA datasets. Best results are shown in **bold**.

Dataset	Method	DSC ↑	clDice ↑	HD95 (mm) ↓
ICA	UNet2D+$\mathcal{L}_{\text{base}}$	.8839 ± .0063	.8788 ± .0058	6.53 ± .38
	UNet2D+$\mathcal{L}_{\text{UQ}}$	.8816 ± .0084	.8760 ± .0082	6.65 ± .42
	UNet2D+$\mathcal{L}_{\text{UQ}}$ + UGCP	**.8890 ± .0047**	**.8811 ± .0057**	**6.32 ± .35**
ICA	SwinUNetR2D+$\mathcal{L}_{\text{base}}$	.8759 ± .0104	.8651 ± .0076	7.88 ± .67
	SwinUNetR2D+$\mathcal{L}_{\text{UQ}}$+ UGCP	.8803 ± .0076	.8697 ± .0065	7.60 ± .64
CCTA	UNet3D+$\mathcal{L}_{\text{base}}$	.8147 ± .0051	.8553 ± .0038	8.89 ± .56
	UNet3D+$\mathcal{L}_{\text{UQ}}$	.8105 ± .0039	.8488 ± .0072	9.07 ± .51
	UNet3D+$\mathcal{L}_{\text{UQ}}$+UGCP	.8188 ± .0040	.8585 ± .0045	8.76 ± .43
CCTA	SwinUNetR3D+$\mathcal{L}_{\text{base}}$	.8160 ± .0067	.8513 ± .0079	8.83 ± .60
	SwinUNetR3D+$\mathcal{L}_{\text{UQ}}$+ UGCP	**.8189 ± .0064**	**.8601 ± .0035**	**8.56 ± .42**

case, and sliding-window inference with overlap 0.5 is adopted. Five-fold cross-validation is employed for all experiments, and mean±standard deviation are reported. Evaluation metrics include Dice similarity coefficient (DSC), centerline Dice (clDice), and 95th percentile Hausdorff distance (HD95).

We evaluate the convolution-based UNet [19] and the Transformer-based SwinUNetR [8] as backbones, i.e. $\mathcal{B}$. UGCP is further integrated with each backbone model to construct the proposed segmentation framework, without altering the original architectural design. All models are trained for 400 epochs using Adam with initial learning rate 10^{-3}, weight decay 10^{-4}, cosine scheduling, and batch size 4. Early stopping with patience 50 is applied based on validation DSC. Unless otherwise stated, all hyperparameters are shared across 2D and 3D experiments. We set the number of update steps to $T = 2$ to balance local correction, over-propagation risk, and computational cost. The uncertainty threshold, temperature, and step size are set to $u_0 = 0.5$, $\tau = 0.1$, and $\theta = 1$, respectively.

Baseline segmentation methods are optimized using

$$\mathcal{L}_{\text{base}} = \mathcal{L}_{\text{Dice}} + \mathcal{L}_{\text{BCE}}, \tag{8}$$

where $\mathcal{L}_{\text{Dice}}$ denotes Dice loss and $\mathcal{L}_{\text{BCE}}$ denotes binary cross-entropy loss. To incorporate evidential uncertainty modeling, we adopt a Dirichlet-based objective defined as

$$\mathcal{L}_{\text{UQ}} = \mathcal{L}_{\text{Dice}} + \mathcal{L}_{\text{NLL}} + \frac{1}{2}\mathcal{L}_{\text{KL}}, \tag{9}$$

where $\mathcal{L}_{\text{NLL}}$ denotes the negative log-likelihood computed from the Dirichlet expected class probabilities, and $\mathcal{L}_{\text{KL}}$ denotes the Kullback–Leibler divergence between the predicted Dirichlet distribution $\text{Dir}(\alpha^{(T)})$ and a uniform Dirichlet prior $\text{Dir}(1)$, which regularizes the evidence parameters. UGCP relies on the uncertainty field derived from evidential modeling and is therefore trained under $\mathcal{L}_{\text{UQ}}$.

3.2 Results and Analysis

Table 1 summarizes quantitative results on 2D ICA and 3D CCTA datasets. UGCP consistently improves DSC and clDice while reducing HD95 across both

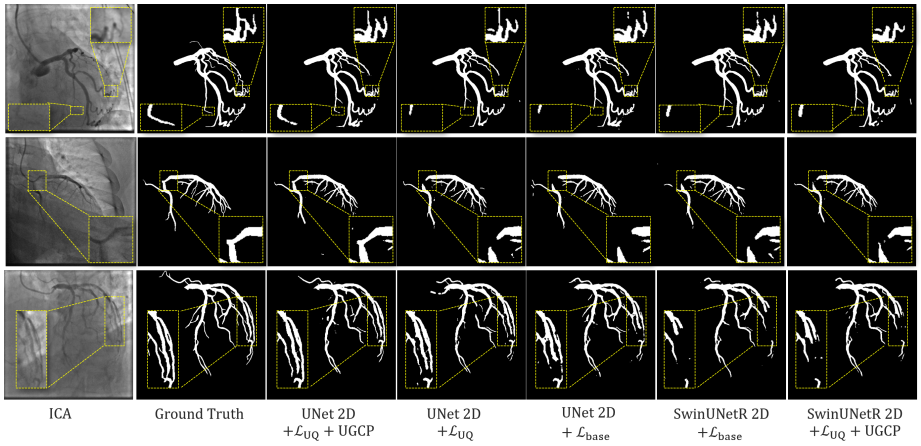

Fig. 2. Comparison of segmentation results on the 2D ICA dataset. Regions susceptible to coronary artery discontinuity are highlighted for detailed comparison.

Table 2. Component ablation study of UGCP on 2D ICA using UNet 2D as the backbone.

UQ Gate	Edge Factor	Source Term	DSC ↑	clDice ↑	HD95 (mm) ↓
×	×	×	.8782 ± .0091	.8691 ± .0082	7.10 ± .44
✓	×	×	.8834 ± .0086	.8766 ± .0087	6.64 ± .41
✓	✓	×	.8869 ± .0095	.8783 ± .0064	6.50 ± .39
✓	✓	✓	**.8890 ± .0047**	**.8811 ± .0057**	**6.32 ± .35**

UNet and SwinUNetR backbones. On 2D ICA, DSC increases by 0.51 and 0.44 percentage points for UNet 2D and SwinUNetR 2D, respectively. On 3D CCTA, DSC increases by 0.41 and 0.29 percentage points for UNet 3D and SwinUNetR 3D, respectively. The consistent clDice improvement, especially from 0.8513 to 0.8601 on SwinUNetR 3D, indicates improved centerline-level structural consistency. In contrast, the Dirichlet-based uncertainty objective alone does not yield comparable improvements, suggesting that uncertainty modeling is most effective when coupled with structured inference updating.

Figures 2 and 3 present qualitative comparisons on the 2D ICA and 3D CCTA datasets. Baseline predictions exhibit branch fragmentation, spurious connections, and ambiguous boundaries. UGCP produces more continuous arterial structures with fewer false positives and clearer boundary delineation, particularly in thin-vessel regions.

Table 2 reports the component ablation study on the 2D ICA dataset. Using the update without the UQ gate, edge factor, and source term results in the lowest performance, indicating that propagation without uncertainty and structural modulation is insufficient. Enabling the UQ gate yields a clear performance improvement, highlighting the importance of uncertainty-guided regulation. Further incorporating the edge factor and source term leads to progressive gains in DSC and clDice, together with consistent reductions in HD95. The full config-

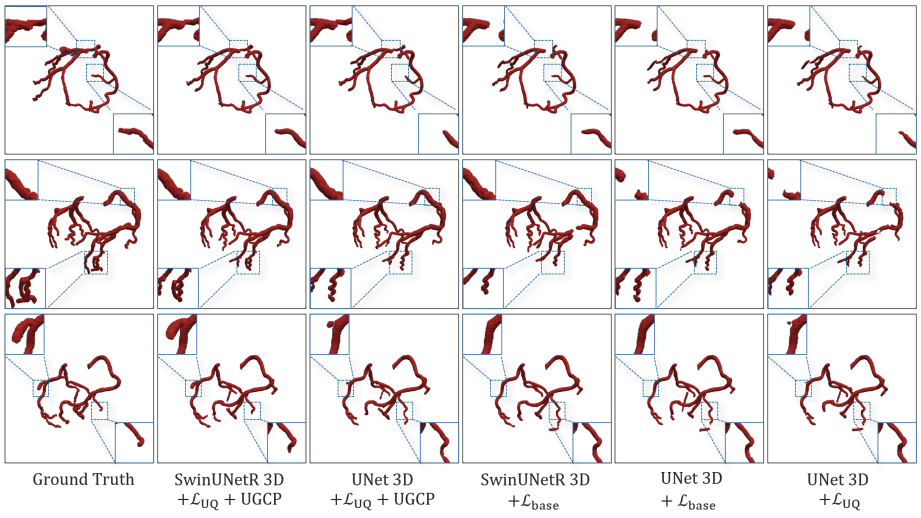

Fig. 3. Comparison of segmentation results on the 3D CCTA dataset. Regions susceptible to coronary artery discontinuity are highlighted for detailed comparison.

uration achieves the best overall performance with reduced variance, suggesting that uncertainty modulation, structural interaction, and source stabilization play complementary roles in producing stable and structurally coherent predictions.

4 Conclusion

Coronary artery segmentation remains challenging due to thin, elongated vessels and delicate structural dependencies. This work reformulates segmentation inference as a structured logit-space update process and introduces uncertainty-guided conservative-inspired propagation for controlled local refinement. Experiments on 2D ICA and 3D CCTA datasets demonstrate consistent improvements across convolutional and Transformer-based backbones, while ablation analysis verifies the complementary roles of uncertainty modulation, structural interaction, and source stabilization. These findings suggest the value of structured inference mechanisms for improving structural consistency in computer-aided cardiovascular analysis. Future work will further investigate topology-specific behavior, comparisons with classical and tubular-structure refinement methods, and efficiency and sensitivity in broader cardiovascular analysis scenarios.

Acknowledgments. This work was partially supported by the American Heart Association under AIREA Award No. 25AIREA1377168.

Disclosure of Interests. The authors have no competing interests to declare.

References

1. Bruns, S., Wolterink, J.M., van den Boogert, T.P., Runge, J.H., Bouma, B.J., Henriques, J.P., Baan, J., Viergever, M.A., Planken, R.N., Išgum, I.: Deep learning-based whole-heart segmentation in 4d contrast-enhanced cardiac ct. Computers in biology and medicine **142**, 105191 (2022)
2. Chen, F., Li, S., Wei, C., Zhang, Y., Guo, K., Zheng, Y., Cao, F., Liang, J.: Positive-unlabeled learning for coronary artery segmentation in ccta images. Biomedical Signal Processing and Control **87**, 105473 (2024)
3. Das, N., Das, S.: Attention-unet architectures with pretrained backbones for multi-class cardiac mr image segmentation. Current problems in cardiology **49**(1), 102129 (2024)
4. El-Taraboulsi, J., Cabrera, C.P., Roney, C., Aung, N.: Deep neural network architectures for cardiac image segmentation. Artificial Intelligence in the Life Sciences **4**, 100083 (2023)
5. Faghani, S., Moassefi, M., Rouzrokh, P., Khosravi, B., Baffour, F.I., Ringler, M.D., Erickson, B.J.: Quantifying uncertainty in deep learning of radiologic images. Radiology **308**(2), e222217 (2023)
6. Föllmer, B., Biavati, F., Wald, C., Stober, S., Ma, J., Dewey, M., Samek, W.: Active multitask learning with uncertainty-weighted loss for coronary calcium scoring. Medical physics **49**(11), 7262–7277 (2022)
7. Gharleghi, R., Chen, N., Sowmya, A., Beier, S.: Towards automated coronary artery segmentation: A systematic review. Computer Methods and Programs in Biomedicine **225**, 107015 (2022)
8. He, Y., Nath, V., Yang, D., Tang, Y., Myronenko, A., Xu, D.: Swinunetr-v2: Stronger swin transformers with stagewise convolutions for 3d medical image segmentation. In: International Conference on Medical Image Computing and Computer-Assisted Intervention. pp. 416–426. Springer (2023)
9. Huang, H., Qiu, L., Yang, S., Li, L., Nan, J., Li, Y., Han, C., Zhu, F., Zhao, C., Zhou, W.: 3d lymphoma segmentation on pet/ct images via multi-scale information fusion with cross-attention. Medical Physics **52**(6), 4371–4389 (2025)
10. Kaba, Ş., Haci, H., Isin, A., Ilhan, A., Conkbayir, C.: The application of deep learning for the segmentation and classification of coronary arteries. Diagnostics **13**(13), 2274 (2023)
11. Li, Y., Wu, Y., He, J., Jiang, W., Wang, J., Peng, Y., Jia, Y., Xiong, T., Jia, K., Yi, Z., et al.: Automatic coronary artery segmentation and diagnosis of stenosis by deep learning based on computed tomographic coronary angiography. European Radiology **32**(9), 6037–6045 (2022)
12. Liu, J., Zhang, X., Gu, D., Ouyang, X., Zhang, J., He, X., Shen, D., Xue, Z.: Semi-supervised domain-adaptive pulmonary artery segmentation via uncertainty guidance and shape strengthening. In: 2023 IEEE 20th International Symposium on Biomedical Imaging (ISBI). pp. 1–4. IEEE (2023)
13. Martín-Isla, C., Campello, V.M., Izquierdo, C., Kushibar, K., Sendra-Balcells, C., Gkontra, P., Sojoudi, A., Fulton, M.J., Arega, T.W., Punithakumar, K., et al.: Deep learning segmentation of the right ventricle in cardiac mri: the m&ms challenge. IEEE Journal of Biomedical and Health Informatics **27**(7), 3302–3313 (2023)
14. Mehrtash, A., Wells, W.M., Tempany, C.M., Abolmaesumi, P., Kapur, T.: Confidence calibration and predictive uncertainty estimation for deep medical image segmentation. IEEE transactions on medical imaging **39**(12), 3868–3878 (2020)

15. Mi, Y., Ren, P., Xu, H., Liu, H., Wang, Z., Guo, Y., Wen, J.R., Sun, H., Liu, Y.: Conservation-informed graph learning for spatiotemporal dynamics prediction. In: Proceedings of the 31st ACM SIGKDD Conference on Knowledge Discovery and Data Mining V. 1. pp. 1056–1067 (2025)
16. Nannini, G., Saitta, S., Baggiano, A., Maragna, R., Mushtaq, S., Pontone, G., Redaelli, A.: A fully automated deep learning approach for coronary artery segmentation and comprehensive characterization. APL bioengineering **8**(1) (2024)
17. Ng, M., Guo, F., Biswas, L., Petersen, S.E., Piechnik, S.K., Neubauer, S., Wright, G.: Estimating uncertainty in neural networks for cardiac mri segmentation: a benchmark study. IEEE Transactions on Biomedical Engineering **70**(6), 1955–1966 (2022)
18. Qiu, Y., Li, Z., Wang, Y., Dong, P., Wu, D., Yang, X., Hong, Q., Shen, D.: Corsegrec: a topology-preserving scheme for extracting fully-connected coronary arteries from ct angiography. In: International Conference on Medical Image Computing and Computer-Assisted Intervention. pp. 670–680. Springer (2023)
19. Ronneberger, O., Fischer, P., Brox, T.: U-net: Convolutional networks for biomedical image segmentation. In: International Conference on Medical image computing and computer-assisted intervention. pp. 234–241. Springer (2015)
20. Sensoy, M., Kaplan, L., Kandemir, M.: Evidential deep learning to quantify classification uncertainty. Advances in neural information processing systems **31** (2018)
21. Song, A., Xu, L., Wang, L., Wang, B., Yang, X., Xu, B., Yang, B., Greenwald, S.E.: Automatic coronary artery segmentation of ccta images with an efficient feature-fusion-and-rectification 3d-unet. IEEE journal of biomedical and health informatics **26**(8), 4044–4055 (2022)
22. Tsai, T.Y., Lin, L., Hu, S., Tsao, C.W., Li, X., Chang, M.C., Zhu, H., Wang, X.: Uu-mamba: Uncertainty-aware u-mamba for cardiovascular segmentation. arXiv e-prints pp. arXiv–2409 (2024)
23. Xiong, X., Zhang, X., Jiang, C., Liu, J., Cui, Z., Wu, D., Shen, D.: Discontinuity-aware coronary artery segmentation on ccta image. In: 2024 IEEE International Symposium on Biomedical Imaging (ISBI). pp. 1–5. IEEE (2024)
24. Yan, Z., Su, Y., Sun, H., Yu, H., Ma, W., Chi, H., Cao, H., Chang, Q.: Segnet-based left ventricular mri segmentation for the diagnosis of cardiac hypertrophy and myocardial infarction. Computer Methods and Programs in Biomedicine **227**, 107197 (2022)
25. Yang, X., Xu, L., Yu, S., Xia, Q., Li, H., Zhang, S.: Segmentation and vascular vectorization for coronary artery by geometry-based cascaded neural network. IEEE Transactions on Medical Imaging **44**(1), 259–269 (2024)
26. Zeng, A., Wu, C., Lin, G., Xie, W., Hong, J., Huang, M., Zhuang, J., Bi, S., Pan, D., Ullah, N., et al.: Imagecas: A large-scale dataset and benchmark for coronary artery segmentation based on computed tomography angiography images. Computerized Medical Imaging and Graphics **109**, 102287 (2023)
27. Zhang, X., Sun, K., Wu, D., Xiong, X., Liu, J., Yao, L., Li, S., Wang, Y., Feng, J., Shen, D.: An anatomy-and topology-preserving framework for coronary artery segmentation. IEEE Transactions on Medical imaging **43**(2), 723–733 (2023)
28. Zhang, Y., Luo, G., Wang, W., Cao, S., Dong, S., Yu, D., Wang, X., Wang, K.: Ttn: topological transformer network for automated coronary artery branch labeling in cardiac ct angiography. IEEE Journal of Translational Engineering in Health and Medicine **12**, 129–139 (2023)
29. Zhao, C., Vij, A., Malhotra, S., Tang, J., Tang, H., Pienta, D., Xu, Z., Zhou, W.: Automatic extraction and stenosis evaluation of coronary arteries in invasive coronary angiograms. Computers in biology and medicine **136**, 104667 (2021)